Adver

Research Article | 🔓 Full Access

Unraveling an Innate Mechanism of Pathological Mineralization-Regulated Inflammation by a Nanobiomimetic System

Dongyang Wang, Xiaomeng Wang, Lei Huang, Ziyi Pan, Kexuan Liu, Beibei Du, Ying Xue, Bei Li, Yuan Zhang ✉, Huan Wang ✉, Daowei Li ✉, Hongchen Sun

Abstract

Pathological mineralization (PTM) often occurs under inflammation and affects the prognosis of diseases, such as atherosclerosis and cancers. However, how the PTM impacts inflammation has not been well explored. Herein, poly lactic-*co*-glycolic acid (PLGA)/gelatin/hydroxyapatite (HA) electrospun nanofibers are rationally designed as an ideal PTM microenvironment biomimetic system for unraveling the role of PTM on inflammation. The results demonstrate that the inflammatory response decreases continuously during the process of mineralization. When mature macromineralization forms, the inflammation almost completely disappears. Mechanistically, the PTM formation is mediated by matrix proteins, local high calcium, and cell debris (nuclei), or actively regulated by the lysosomal/plasma membrane components secreted by macrophages. These inflammatory inducible factors (calcium, cell debris, etc.) can be "buried" through PTM process, resulting in reduced immune responses. Overall, the present study demonstrates that PTM is an innate mechanism of inflammation subsidence, providing valuable insight into understanding the action of mineralization on inflammation.

1 Introduction

Pathological mineralization (PTM) is characterized by calcium phosphate salts deposition and almost all connective tissues can suffer from mineralization. PTM often occurs in cancer (thyroid carcinoma, breast cancer, and meningioma),[1, 2] cardiovascular diseases,[3] osteoarthritis (OA),[4] and aging conditions.[5] It is noteworthy that PTM often occurs under inflammation and affects the prognosis of various diseases. For instance, breast cancers with

mineralization formation exhibit a worse prognosis than the conditions without mineralization. [6] In joints, PTM is often occurred during OA, leading to the formation of osteophytes, which is regarded as the major cause of joint movement limitation and pain.[7] In arteries, mineralization increases atherosclerotic plaque burden, which is associated with a higher risk of myocardial infarction. Medial arterial mineralization can facilitate cardiovascular events in diabetic patients and is a strong independent pathogenic element in these patients. In the heart, valves are also particularly susceptible to mineralization. Degenerative calcific aortic stenosis is the most common clinical cardiological disease and is particularly difficult to manage.[8] Thus, mineralization-associated diseases are worldwide problems that endanger human health.

Generally, the sustained inflammatory response seems to be a key factor during the pathological mineralization in soft tissues. Inflammation has long been associated with the development of cancer.[9] Cancer mineralization in the breast can occur in necrotic debris, with inflammation being plausible mediator.[10] In the vasculature, the chronic inflammatory focus has been demonstrated to be sites of atherosclerotic mineralization in human and animal model, suggesting that the atherosclerotic mineralization arises from chronic inflammation.[11, 12] Moreover, the activation of the synovial lining macrophage (synovitis) is frequently recognized in OA joints.[13] The formation of osteophytes at the junction of synovium and periosteum is a general feature.[14] In modern armed conflict, ectopic mineralization is also a common complication of the high-energy extremity trauma. Serum and effluent analysis from combat wounds suggests that the profiles of dysregulated inflammatory signaling may drive ectopic mineralization formation.[15]

Ectopic mineralization is a dynamic process that is regulated and controlled by multiple factors, mainly including calcium and phosphate, proteins, lipid, and local infiltrated cells etc.[8] However, the specific function of each of these factors are not well understood. Among them, monocyte and macrophage are involved in almost all the stages of the mineralization process. [11] Targeting tumor necrosis factor through monoclonal antibody infliximab blocks mineralization in LDLR deficient mice.[16] In addition, the exosome-like extracellular vesicles secreted by macrophages can also promote mineralization in patients.[17] Nevertheless, during the progression of mineralization, the role of PTM is not well defined. It is unclear whether PTM acts as an initiator or an inhibitor of inflammation.[17-19] Besides, there is still a lack of good in vivo model to investigate the action of mineralization on inflammation in healthy individuals without the interference of major diseases, such as genetic disorders, important organ disorders, and immune function defects etc.

In the present study, an extracellular matrix (ECM)-like PLGA/gelatin/hydroxyapatite electrospun nanofibers were rationally designed as an ideal PTM microenvironment biomimetic system for unraveling the role of PTM on inflammatory responses in vivo. In this system, PLGA,

gelatin, and hydroxyapatite were used to simulate the PTM microenvironment with high content of lipid, matrix proteins, and calcium ions. As an aliphatic polyester, PLGA could mimic lipids, induce local inflammation and promote the formation of scattered spotty mineralization but would prevent calcium ion penetration. Gelatin could mimic matrix proteins, promote calcium ion permeation, nucleation, and crystal maturation, forming a more stable mineralization. Our results indicated that the inflammatory response decreases continuously during the process of mineralization. When mature macro-mineralization forms, the inflammation almost completely disappears (**Figure** 1a). Mechanistically, the PTM formation is passively mediated by matrix proteins, local high calcium, and cell debris (nuclei), or actively regulated by the lysosome/plasma membrane components secreted by macrophages. These inflammatory inducible factors (calcium ions, cell debris, membrane components) can be "buried" during the PTM process, leading to subsided immune responses. This study will not only provide valuable insight into the understanding of mineralization but also facilitate the development of novel therapeutics for mineralization-associated diseases via reasonably regulating the degree of local mineralization.
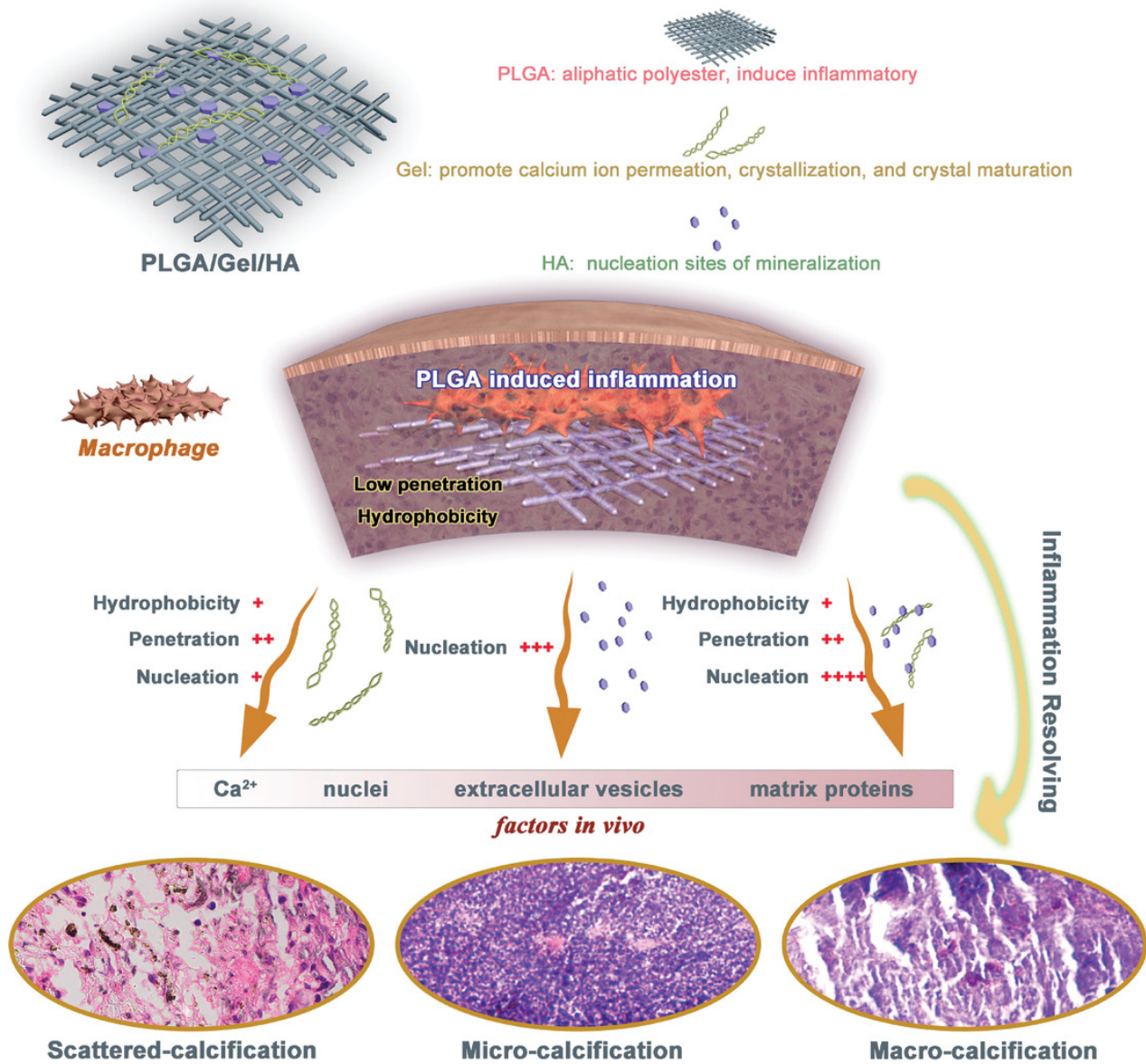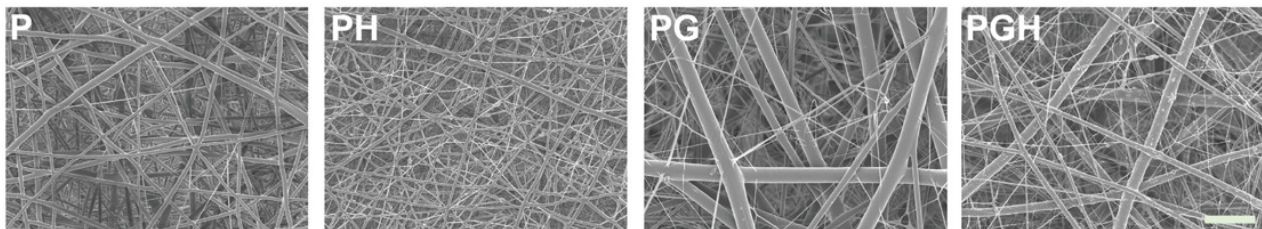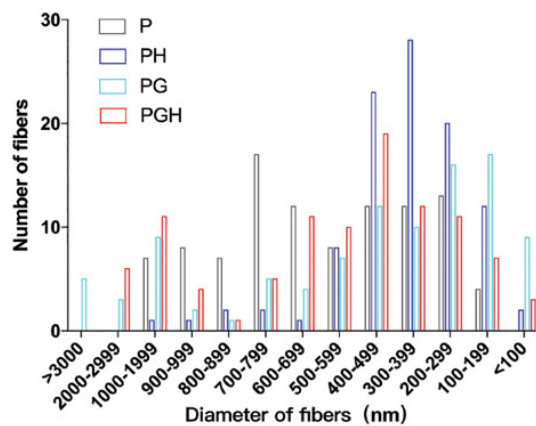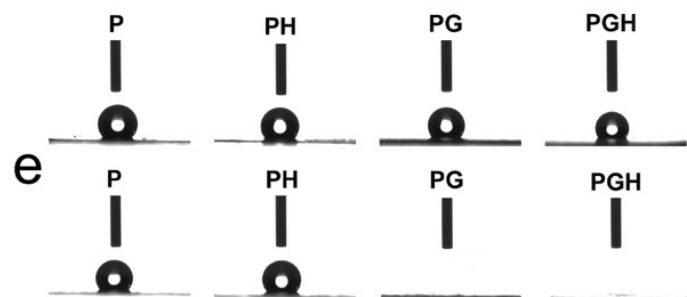
Figure 1

a) Schematic illustration of the pathological mineralization-mediated inflammation subsidence in vivo. b) Typical SEM images of the PLGA (P), PLGA/Hydroxyapatite (PH), PLGA/Gelatin (PG), and PLGA/Gelatin/Hydroxyapatite (PGH) nanofibrous scaffolds. c) The diameter distributions of the nanofibers. Contact angle analysis of various scaffolds e) with or d) without the preimmersion in water.

2 Results and Discussion

2.1 Characterization of Nanofibrous Scaffolds

The PLGA (P), PLGA/gelatin (PG), PLGA/hydroxyapatite (PH), and PLGA/gelatin/hydroxyapatite (PGH) nanofibrous scaffolds were prepared via electrospinning, and their morphologies were characterized by SEM. As shown in Figure 1, all the scaffolds presented randomly oriented morphology. The HA nanoparticles were well dispersed on the surface of the PH and PGH nanofibers. Compared with the group of P and PG, decreased fiber diameters were found in the group of PH and PGH when HA was added. Moreover, coarse-diameter fibers and fine-diameter fibers appeared simultaneously in PG and PGH groups which contained gelatin. The results indicated a significant effect of phase separation on the structure of electrospun nanofibers.[20]

The contact angle can reflect the wettability of the material surface. As shown in Figure 1d,e and Table S2 (Supporting Information), there was a negligible difference among the contact angles of various groups when liquid was dropped on the surface of the scaffolds at the beginning. Although gelatin and hydroxyapatite were considered as hydrophilic components, the hydrophilic/hydrophobic nature of the nanofibrous scaffold was also dependent on their surface structure.[21] Our results showed that the porous fibrous surface could hold droplets at the beginning (Figure 1d). However, if the scaffolds were pre-immersed in water, the contact angle of gelatin-contained scaffolds could not be detected, indicating that the gelatin-contained scaffolds showed excellent hydrophilicity and water penetration under such condition (Figure 1e). Besides, the water uptake ratio of the scaffold could reflect its permeability and hydrophilicity. The water uptake ratios of gelatin contained nanofibrous scaffolds (PG and PGH) were significantly higher than those in the groups of P and PH. The swelling ratios of PG and PGH composite scaffolds were determined to be 301 ± 11.3% and 302 ± 20.4% respectively. The excellent water uptake ability implied that the fluid could permeate well in and out of the gelatin-contained scaffolds in vivo (Table S3, Supporting Information).

2.2 Histological Analysis of PTM In Vivo

Representative H&E sections of the tissues implanted with various nanofibers were shown in **Figure** 2a. The results showed that there was obvious mineralization in PH and PGH groups at the junction of scaffolds and tissue, building a "mineral wall" to separate the inner part of scaffolds with surrounding tissues. Besides, it could be found that the basophilia stain of HA was much stronger at the interface of scaffolds and tissues compared with that at the inner part of scaffolds, indicating that the body fluid and cells significantly contributed to the mineralization around the scaffolds. In contrast, no mineralization could be identified in the groups of P and PG according to the H&E sections. These results indicated that the excessive calcium accumulation and nucleation are critical for PTM. Notably, the nano-HA could act as nucleation sites for further mineralization. Thus, the inhibition of calcium deposition and nucleation would be effective for preventing mineralization in mineralized sites.
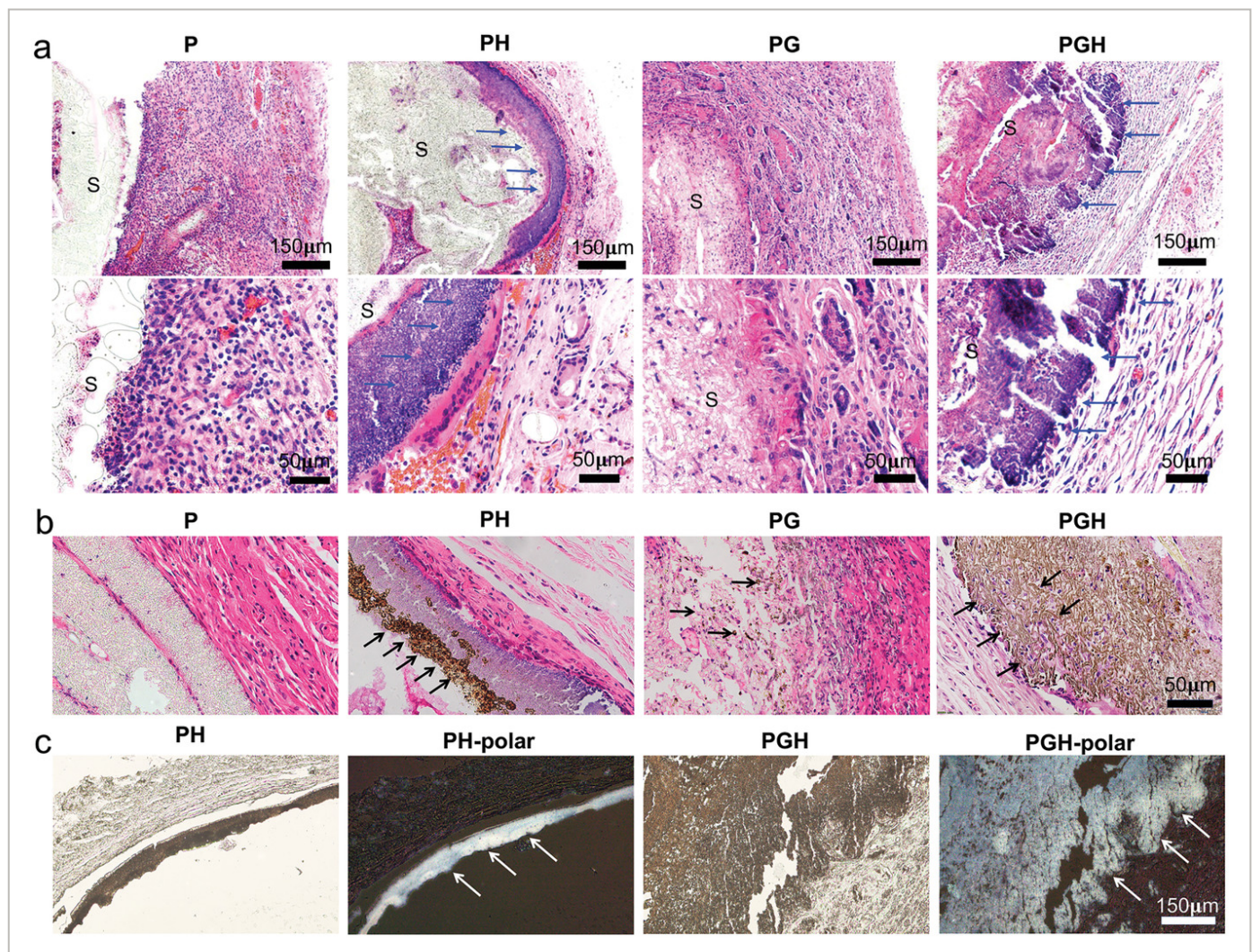

Figure 2

Open in figure viewer | PowerPoint

Nanofibrous scaffolds-mediated mineralization in vivo. a) Typical hematoxylin-eosin staining images, b) Von Kossa staining images, and c) polarizing microscope images of tissue sections in various groups. Black arrows indicate positive staining of

mineralization. White arrows indicate crystallized mature mineralization with light transmittance property. Abbreviations: S, scaffold remnants; P, PLGA; PH, PLGA/Hydroxyapatite; PG, PLGA/Gelatin; and PGH, PLGA/Gelatin/Hydroxyapatite.

Furthermore, we could find that the morphology of mineralization in PGH group was plate-like which was similar to the macromineralization in atherosclerosis patients (Figure 2a).[22] However, the group of PH exhibited granular mineralization which was similar to the micromineralization in atherosclerosis patients. The plate-like macro mineralization indicated high level of crystallization, while granular morphology indicated a low level of crystallization. These results demonstrated that gelatin could promote the maturity of crystals and form macromineralization, which could be attributed to the good hydrophilicity of gelatin that promoted the penetration and accumulation of calcium ions (Figure 1 and Tables S2 and S3, Supporting Information).[22] Besides, gelatin could serve as the template and framework to guide the mineral deposition and promote the integrity of mineralization. On the other side, the hydrophobic PLGA would prevent calcium ions permeation and integrity of mineralization, leading to the micro-mineralization in PH group. The hydrophobic property and biological effects of PLGA were similar to the fatty deposits in the arterial wall, which triggered local and systemic inflammation.[23] In the clinic, atherosclerosis with micromineralization often has high risk of plaque rupture.[24] Hence, the reduced lipid deposition and the elevated matrix proteins accumulation may promote the formation of mineralization. We postulate that this rule could be utilized to guide the treatment of pathological mineralization-related diseases, such as cardiovascular diseases and OA.[25]

Compared with HA-free groups, the HA contained groups showed significantly more mineralization as indicated by Von Kossa staining images. Moreover, the mineralization depth was deeper in PGH group compared with that in PH group, indicating that gelatin increased the penetration of calcium and phosphate ions into the scaffolds (Figure 2b). Interestingly, we could find that the positive staining blots in PGH and PG groups exhibited needle shape, further indicating that gelatin could serve as the collagen-like template for HA crystal deposition and growth (Figure 2b).[26] Besides, the intensity of stained mineralization in PH group was much higher than that in PGH group, which would be discussed later. In addition, there were some positive staining blots in PG group co-localize with nuclei, demonstrating that the nucleation and mineralization form in situ on the nucleus (Figure 2b, PG group, black arrows).

Polarized light photographs of histological sections on 28 d after implantation (Figure 2c) indicated that the mineralization layer was formed in both PH and PGH groups. We observed a regular band of brightness in direct contact with the surrounding tissues, corresponding to the mineralization area. These results demonstrated that the deposited mineral in PH and PGH groups both had crystalline characteristics.

2.3 Confocal Raman Spectroscopy Analysis of PTM In Vivo

As shown in **Figure** 3b, focusing images of the tissue sections indicated that the mineralized crystals were plate- or rod-like in PGH group, while were spherical shape in PH group. Then, the mineralization states in the tissue sections were investigated by using confocal Raman spectroscopy (Figure 3b). For apatite tissues or synthetic apatite, the Raman-shifted frequency of the $(PO_4)^{-3}$ (ν_1) line was often affected by surrounding minerals. The highly crystalline hydroxyapatite (HA) produces a Raman-shifted frequency in the range of 962 to 964 cm^{-1}. While in the substituted B-type carbonate apatite, the ν_1 Raman-shifted frequency is in the region of 955 to 959 cm^{-1}. A Raman-shifted frequency in the region of 945 to 950 cm^{-1} is indicative of a disordered phosphate lattice of apatite.[27] Hence, the phosphate ν_1 band is a superposition of all three bands and commonly an asymmetric shape due to the influence of vibrations of the HA and the disordered phosphate. Our results showed that a strong Raman peaks at 961 cm^{-1}, corresponding to $(PO_4)^{-3}$ (ν_1), were observed in PG, PH, and PGH group. The results demonstrated that all these scaffolds induced highly crystalline HA formation in vivo. Moreover, the relative intensity of $(PO_4)^{-3}$ (ν_1) was much higher in PGH group compared with other groups. The phosphate ν_1 band is asymmetric shape due to the incorporation of a Raman peak at 945 cm^{-1} [disordered phosphate lattice of apatite] in PG, PH, and PGH group (Figure 3c). The relative intensity ratio of the $(PO_4)^{-3}$ (ν_1) peaks at 961 cm^{-1} to 945 cm^{-1} was the highest in PGH group (I_{961} /I_{945} = 2.12) compared to other groups, which meant more highly crystalline HA was formed (Figure 3c). However, the intensity of peaks of B-type carbonate at 1071 cm^{-1} was similar among the four groups. These results demonstrated that the increase of crystallization in PGH group was independent of B-type carbonate substitution. It is well known that B-type carbonate substituted HA is commonly occurred in human bone mineral and plays a significant role in bone metabolism.[28] This could be attributed to the fact that the initial deposition of HA mineral is formed at the inner portion of the matrix vesicles (MV) membrane of osteoblasts. Besides, carbonic anhydrase (CA), as a powerful catalyst for the reversible hydration of carbon dioxide, is also abundantly expressed in matrix vesicles.[29, 30] Thus, B-type carbonate substituted HA formation in bone is actively mediated by osteoblasts. Our results demonstrated that highly crystalline HA was tend to be formed during the mineralization process in our model, which was essentially different from bone mineralization on account of different forming mechanisms. The highly crystalline HA should be originated from the local high concentration of calcium ions and phosphate as well as the lack of necessary components for the formation of B-type carbonate substituted HA. Although studies had reported that several different types of cells, such as myocytes, have the tendency to differentiate into osteoblasts, it may just be an adaptive response.[31] Moreover, the relative intensity of $(PO_4)^{-3}$ (ν_1) was much higher in PGH group compared with other groups, indicating that more stable mature hydroxyapatite crystals (macro-mineralization) were formed in PGH group. Compared with immature hydroxyapatite crystals, mature hydroxyapatite crystals with larger sizes

showed smaller specific surface area and thus fewer calcium exposure sites. Therefore, the intensity of stained mineralization in PH group was higher than that in PGH group in the von Kossa staining images (Figure 2b).
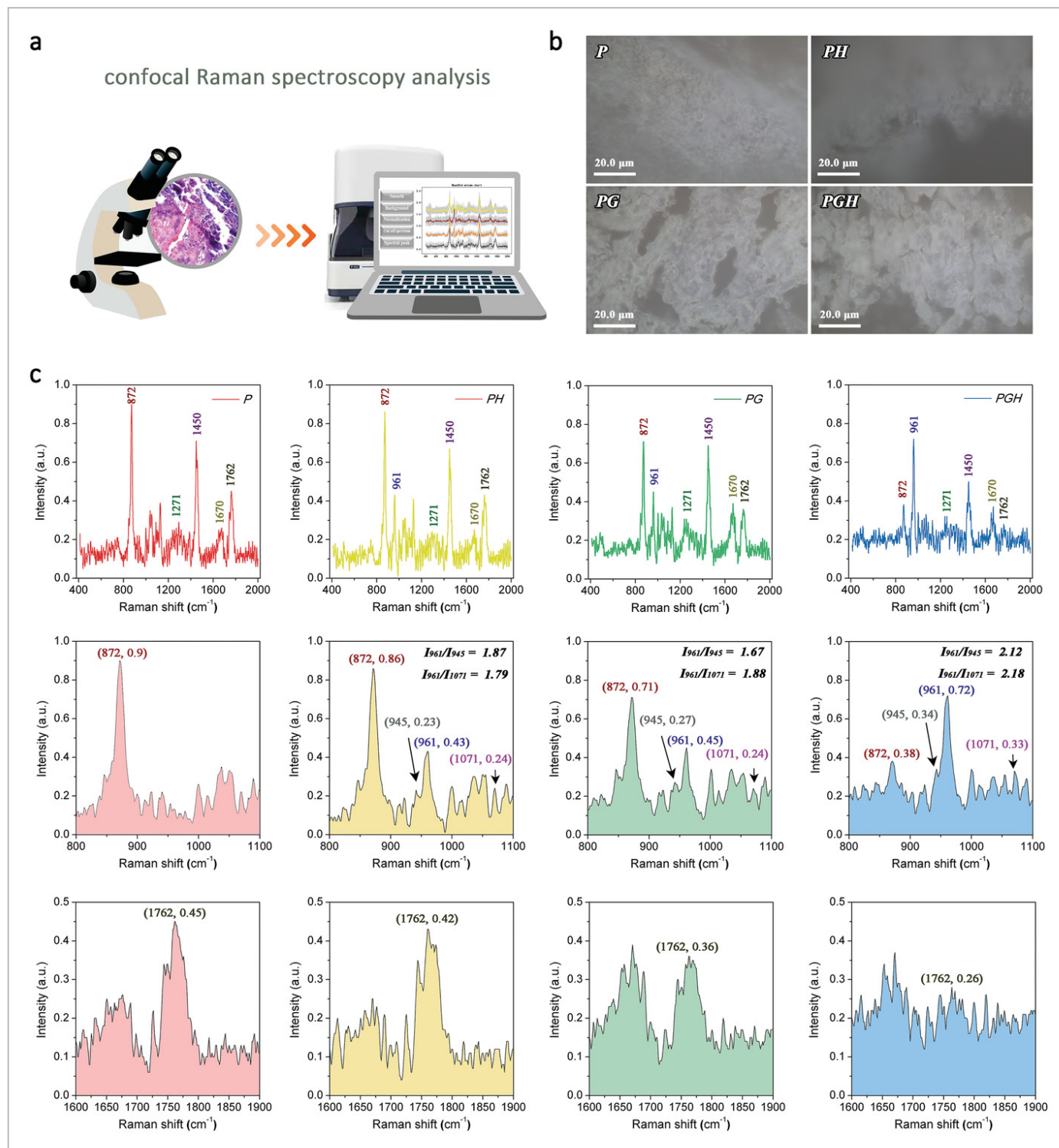

Figure 3

Open in figure viewer   ⬇PowerPoint

Confocal Raman spectroscopy analysis. a) Schematic illustration of the confocal Raman spectroscopy analysis of tissue sections. b) Focusing images of tissue sections in various groups under upright microscope. c) Raman spectra of tissue sections at 28 days post-implantation of various treatments . Abbreviations: S, scaffold remnants; P, PLGA; PH, PLGA/Hydroxyapatite; PG, PLGA/Gelatin; and PGH, PLGA/Gelatin/Hydroxyapatite. PO_4^{-3} in highly crystalline HA, 962–964 cm^{-1}; PO_4^{-3} in B-type carbonate apatite, 955–959 cm^{-1}; PO_4^{-3} in disordered phosphate lattice of apatite, 955–959 cm^{-1}; B-type carbonate, 1071 cm^{-1}; C—COO in lactic acid, 872 cm^{-1}; anti-symmetric of CH_3, 1450 cm^{-1}; the ester bonds in PLGA, 1762 cm^{-1}; Amide I (1670 cm^{-1}) and Amide III (1271 cm^{-1}) in Gelatin.

For PLGA or gelatin, the characteristic Raman shifted frequencies were shown in Figure 3c. All the spectrums contained Raman peaks at 872 ($\nu_{C—COO}$), 1450 (δ_{CH3}) and 1762 ($\nu_{C=O}$) cm^{-1} which were assigned to the stretching of C—COO, antisymmetric of CH_3, and stretching of C=O in PLGA respectively.[32] The Raman-shifted frequency at 1762 cm^{-1} is ester bonds in PLGA. The lower intensity at 1762 cm^{-1} (I_{1762}) in PG and PGH group compared with that in P and PH group demonstrated faster degradation rate of PLGA in these two groups. The results demonstrated that the incorporation of gelatin could promote the degradation of PLGA. This could be attributed to the fact that gelatin could increase the permeability of scaffolds for extracellular fluid and macrophages, facilitating the process of hydrolysis of the ester linkages and/or enzymatic degradation.[33 34] I_{1762} also decreased when HA were incorporated into PLGA. Compared with P and PG scaffolds, decreased fiber diameters were found in the group of PH and PGH when HA was added. Thus, the slightly increased degradation rate of PH scaffolds could be attributed to their larger specific surface area. Notably, the I_{1762} decreased significantly when HA and Gelatin were simultaneously incorporated into PLGA, demonstrating that HA and gelatin could synergistically promote the degradation of PLGA in vivo. Besides, lactic acid was the degradation product of PLGA. The increased permeability and specific surface area could lead to faster degradation of PGH scaffolds, generating more degraded products including lactic acid. The diffusion of the lactic acid was also enhanced in PG and PGH groups because of the higher permeability. Hence, the change of intensity at 872 cm^{-1} (C—COO in lactic acid component) further reconfirmed the degradation characteristic of PLGA in various scaffolds. As a result, the degradation products of PGH scaffolds were mainly lactic acid and glycolic acid for PLGA, calcium ions and phosphate for HA, respectively. The lactic acid and glycolic acid could induce local inflammation microenvironment for PTM formation. And calcium ions and phosphate released from HA could provide a local high concentration for PTM. Additionally, the intensity at 1271 and 1670 cm^{-1} corresponded to the Amide III and Amide I regions of gelatin increased significantly in PG and PGH group due to the incorporation of gelatin.[35] Gelatin could mimic extracellular matrix proteins, providing nucleation sites for PTM formation.

2.4 Mineralization Reduced Immune Responses In Vivo

Histological images of H&E staining showed that all the groups induced different degrees of inflammation due to the acidic degradation product of PLGA (**Figure** 4a). Plenty of macrophages were gathered around the scaffolds in P and PG groups. In contrast, there was significantly lower macrophages infiltration in calcified PGH and PH groups, indicating that the mineralization was closely connected with reduced inflammatory response (Figure 4a). Inflammatory responses score indicated that the PGH and PH group showed lower inflammation, whereas the PG group exhibited the strongest inflammatory response (Figure 4a). This could be attributed to the rapid degradation of PLGA and more acidic products were released in the PG group, as confirmed by the lower intensity of the characteristic Raman peaks of PLGA at 872 (ν_{C-COO}) in PG group (I_{872} = 0.71) compared with that in the PH group (I_{872} = 0.86, Figure 3c).[36] However, the intensity of Raman peaks at 872 (ν_{C-COO}) was as low as 0.38 in the PGH group (Figure 3c), indicating that the degradation rate of PLGA was the fastest in PGH group. In addition, PGH group exhibited mature mineralization while PH group exhibited immature mineralization (Figure 4a). These results demonstrated that the resolution of inflammation was due to mineralization process and its maturation, but not the hydroxyapatite components within the scaffolds. The PTM not only could build a "wall" to restrict the diffuse of acidic product of PLGA, but also could "bury" them in situ. Besides, the major organs of the scaffolds implanted rats showed no obvious pathological change (Figure S2, Supporting Information), which also demonstrated the good biocompatibility of various scaffolds. Thus, the inflammatory response in vivo would be precisely regulated without interference by failure of the major organs.
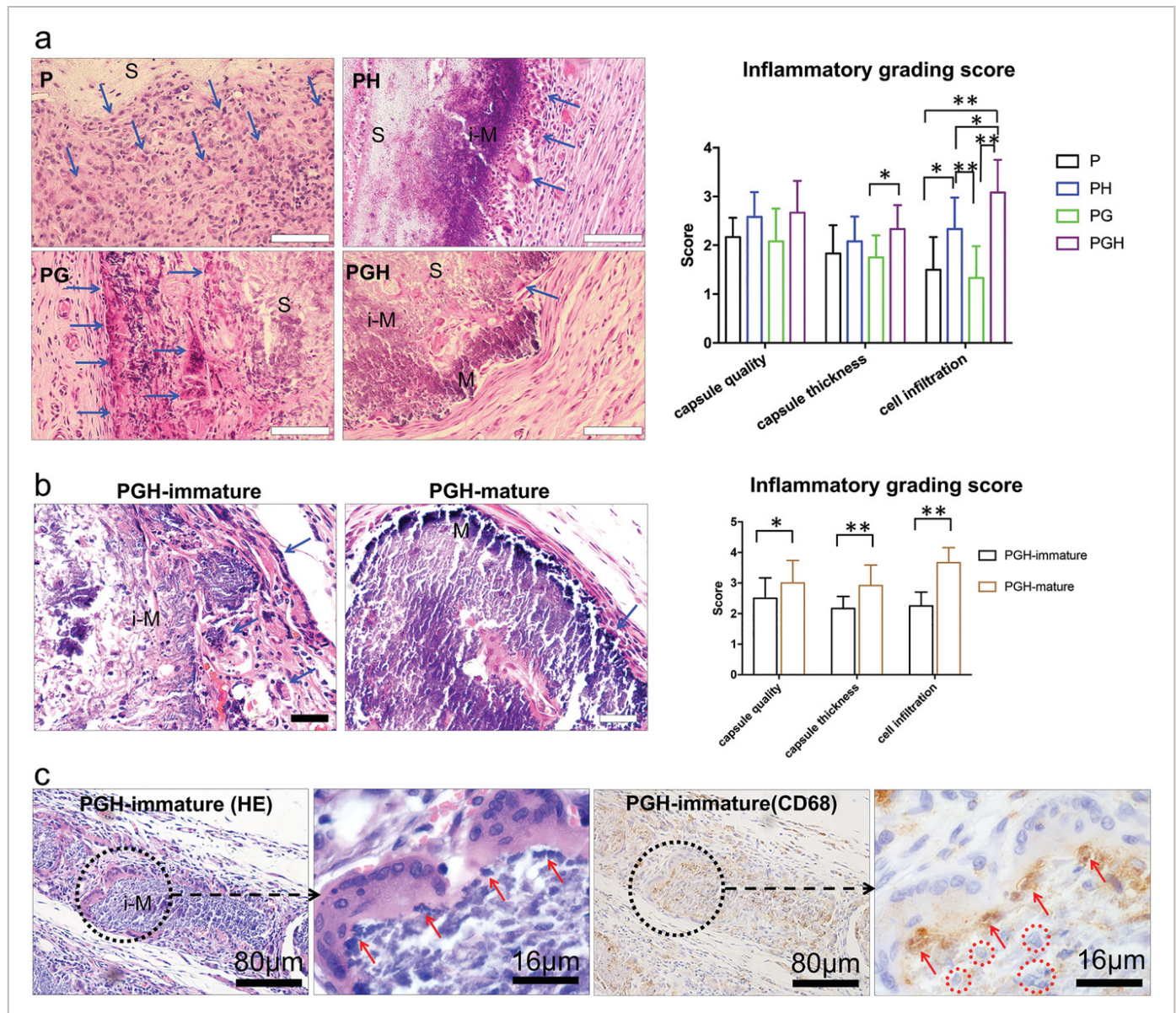
Figure 4

Open in figure viewer | PowerPoint

Immune responses to mineralized scaffolds in vivo. a) Histological analysis of immune responses of tissue sections with various treatments. b) Inflammatory responses under mature and immature mineralized states in the group of PGH. c) The relationship between mineralization and macrophages/nuclei of dead cells. Blue arrows indicate inflammatory cells. Red arrows indicate the co-localization of mineralization with CD68 positive membrane. Red circles indicate the embedded nuclei of dead cells. Abbreviations: P, PLGA; PH, PLGA/Hydroxyapatite; PG, PLGA/Gelatin; and PGH, PLGA/gelatin/hydroxyapatite; S, scaffold remnants; M, mature mineralization; and i-M, immature mineralization. Scale bars in Figure 4a are 50 μm. Scale bars in Figure 4b are 40 μm. Error bars represent standard deviation from the mean (*n* = 4). Asterisks indicate statistically significant differences (*P < 0.05, **P < 0.01, ***P < 0.001).

In PGH group, we could also find immature calcific areas and their inflammatory response was significantly higher than mature calcific areas (Figure 4b). There were even no macrophages infiltrated around the mature calcific area in PGH group. All the calculated scores were significantly higher in mature calcific areas compared with immature areas, especially for cell infiltrations score (3.67 ± 0.49). We also found that the inflammatory scores of immature calcific areas in PGH group were similar to that of immature calcific PH group. The persistent inflammatory of micro-mineralization or immature mineralization may due to the leaking of calcium ions from the mineral and then recruited macrophages. Besides, cell debris may also leak from the micro-mineralization, activate damage associated molecular patterns (DAMPs)[37] mediated inflammatory response.

In Figure 4c, the results showed that immature granular mineralization was surrounded by a layer of multinuclear cells in PGH group. Moreover, the pale brown CD68 immunohistochemistry (IHC) staining blots were colocalized with mineralization, especially at the interfaces of cells and scaffolds as indicated by red arrows in Figure 4c. As we know, CD68 was a lysosomal/plasma membrane shuttling protein.[38] Thus, the colocalization of CD68 with mineralization demonstrated that macrophage could secret membrane components and directly promote mineralization. However, the specific sources of membrane components in cells need further investigation. In addition, we also could find many basophilic nuclei were buried in the mineralization as indicated by blue arrows in Figure 4c. The basophilic nuclei may also contribute to the nucleation and growth of mineralization in PGH group similar to mineralization observed in PG group (Figures 4c and 2b). Thus, the "self-buried" nuclei would not activate inflammatory responses. These results demonstrated that PTM could bury cell debris, such as nuclei and membrane components, to diminish DAMPs associated with inflammation.

In addition, inflammatory cytokines, interleukin α(ILα) and tumor necrosis factor α(TNFα), were also detected by immunohistochemistry staining among various groups. The positive staining of ILα could be found in all the samples of various groups (**Figure** 5a). Strong positive ILα staining was only seen in non-calcified P and PG groups. However, there were few scattered positive ILα staining cells in calcified PGH scaffolds, which was also less than in calcified PH scaffolds (blue arrows, Figure 5a). Besides, there were few positive staining of TNFα among the various groups. These results demonstrated that mineralization could resolve inflammatory responses and was a natural mechanism for the regulation of inflammation in vivo.
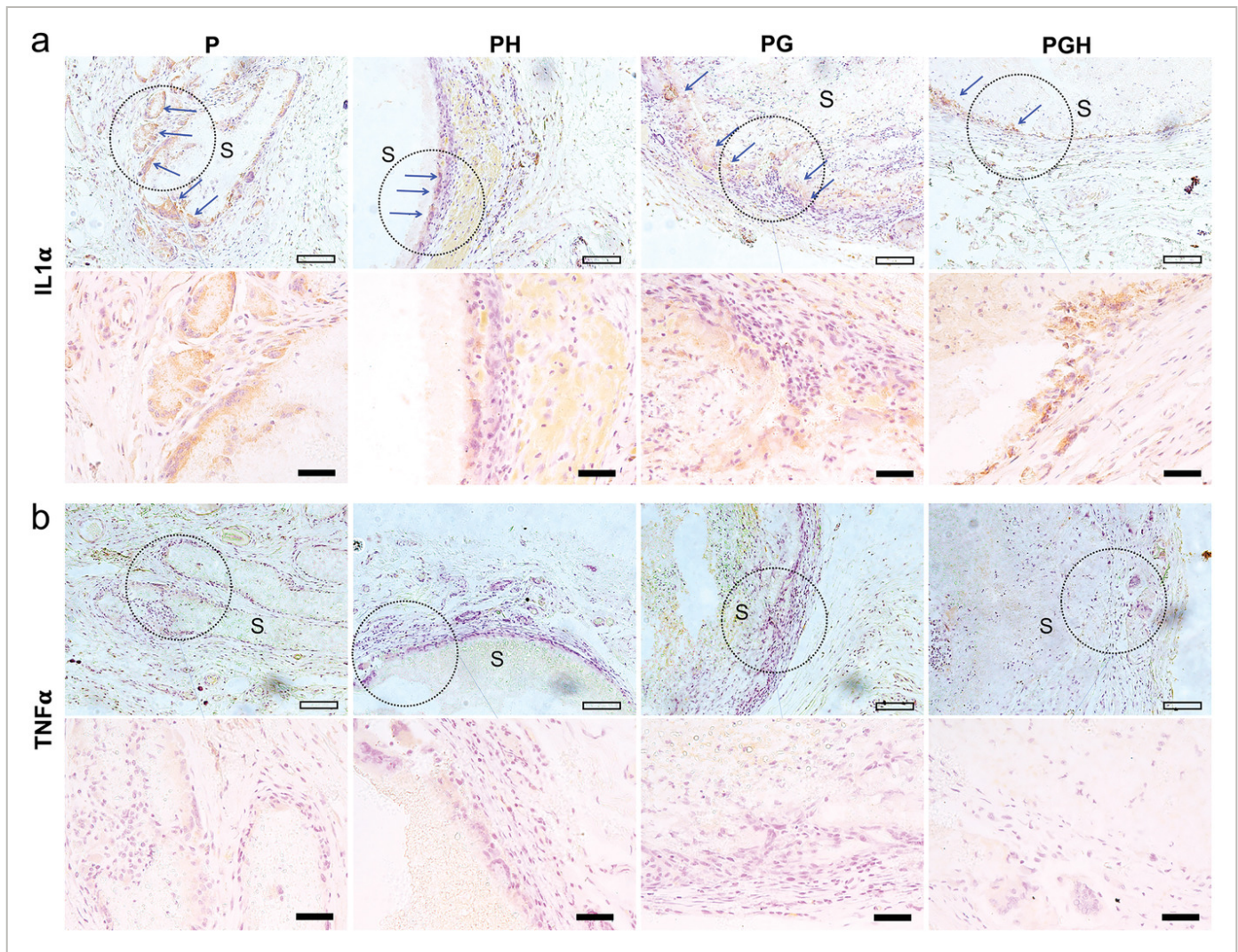
Figure 5

Open in figure viewer | ⬇PowerPoint

Immunohistochemistry staining of ILα and TNFα of tissue sections with various treatments. S: scaffolds remnant, blue arrows indicate positive staining of ILα. Black scale bars were 50 μm. Rectangle scale bars were 100 μm. Abbreviations: P, PLGA; PH, PLGA/hydroxyapatite; PG, PLGA/gelatin; and PGH, PLGA/gelatin/hydroxyapatite.

3 Conclusions

Mineralization associated diseases are worldwide problems that endangers human health and the underlying mechanisms need further investigation. In this study, PLGA/Gelatin/Hydroxyapatite electrospun nanofibers are rationally designed as an ideal PTM microenvironment biomimetic system for unraveling the action of PTM on inflammation. We found that PTM is an innate mechanism of inflammation subsides. PTM resolved inflammatory via "burying" localized inflammatory inducible factors including cell debris, high calcium ions, and membrane components, etc. The role of PTM in regulating inflammation may facilitate the development of novel therapeutics for mineralization-associated diseases by reasonable

regulating the degree of local mineralization, such as diminishing the fatal inflammation in atherosclerosis or high-energy extremity trauma, and turning the immunosuppressive microenvironment in tumor.

4 Experimental Section

Preparation of Scaffolds

PLGA (P), PLGA/HA (PH), PLGA/Gel (PG), and PLGA/Gel/HA (PGH) nanofibrous scaffolds were fabricated via electrospinning method. First, various electrospun solutions were prepared. PLGA electrospun solution was prepared by dissolving PLGA in HFIP of 10% (w/v) concentration. For preparing PH electrospun solution, 0.06g HA and 0.7g PLGA were dispersed in 3 mL and 7 mL HFIP respectively. After stirring for 24 h respectively, the two solutions were mixed and stirred for another 24 h. PG solution was prepared by mixing 0.7 g PLGA and 0.3g Gel in 7 mL and 3mL HFIP respectively. Then, the two solutions were mixed together and stirred for another 24 h. PGH electrospun solution was prepared by adding 0.06 g HA in 3 mL HFIP and stirring for 24 h followed by adding 0.3 g gelatin. Afterwards, the mixtures were stirred for another 24 h. Meanwhile, 0.7 g PLGA was dissolved in 7 mL HFIP and then, mixed them together and stirred for 24 h. The various electrospun solutions were used to prepare nanofibers at 15 kV of high voltage.

Characterization of Scaffolds

The morphology of P, PG, PH, and PGH nanofibrous scaffolds was explored with SEM (SEM; JEOL FESEM 6700F, Tokyo, Japan). The mean size of the fibers and the size distribution were calculated by analyzing 100 fibers from SEM images of the scaffolds by ImageJ software (NIH, Bethesda, MD, USA).

The wettability of P, PG, PH, and PGH fibers was investigated by measuring the sessile drop water contact angle at room temperature (AST products, Billerica, MA). Besides, the swelling ratio of the scaffolds was measured through calculating their water uptake capacity. 5 mg scaffolds (denoted as M1) were put in weighing bottles with 5 mL medium and incubated for 24 h at 37 °C, which could simulate the swelling process in vivo. Then, the scaffolds were placed on filter paper to remove water on the surfaces and weighted (denoted as M2). The equation for calculating swelling ratio was as follows.

$$\text{Swelling ratio}(\%) = (M1 - M2)/M2 \times 100\% \tag{1}$$

The Implantation of Scaffolds In Vivo

Sixteen healthy six-week-old male Wistar rats (≈200g) were used to create dorsal incision model. The protocol was approved by Jilin University Animal Care and Use Committee (NO. 20210642). The rats were randomly divided into four groups. P, PG, PH, and PGH nanofibrous scaffolds were implanted subcutaneously in rats. The animals were anesthetized with isoflurane and Lidocaine (60 mg kg^{-1}) and xylazine (8 mg kg^{-1}) and their backs were shaved and disinfected with 70% ethanol and iodine scrub. Two parallel incisions were made in the paravertebral skin and 1 cm lateral to the vertebral column which was approximately 1 cm long (Figure S1, Supporting Information). The subcutaneous pockets were created by blunt dissection. Both the pockets were implanted on the same scaffold. Finally, 3.0- nylon sutures were used to close the incisions. After the surgery, all rats were received an analgesic and an antibiotic treatment for 3 d. Animals were housed in the same environment and food and water were provided ad libitum.

Sample Preparation and Histological Analysis

At 4 weeks postsurgery, animals were anesthetized and euthanized. The implants and tissue surrounding each implant were harvested intact. The harvested tissues were fixed in 4% paraformaldehyde (Fisher Scientific) for 48 h. The fixed samples were then dehydrated in a graded series of ethanol. Tissue samples were incised along the major axis and embedded in paraffin. Serial sections (3–5 µm) were used for HE staining and histology analysis. The mineralization of P, PG, PH and PGH nanofibrous scaffolds was evaluated by two experienced pathologists under optical microscope (Olympus, Tokyo, Japan).

von Kossa Assay

Von Kossa's method was used to detect the mineral accumulation in the scaffolds. In brief, the paraffin sections were dewaxed and immersed in water, then incubated in 4% silver nitrate solution. Samples were then irradiating under UV light for 30min. After that, samples were washed in distilled water for three times, incubated in 3% sodium thiosulfate pentahydrate solution for 5 min. The samples were then washed in distilled water and stained in Haley's hematoxylin for 5 min. And finally, the samples were stained in Masson staining solution for 2min after washing in distilled water. The stained mineralized scaffolds were observed under optical microscope (Olympus, Tokyo, Japan).

Polarized Light Microscope Observation

Was used to investigate the crystallization of mineralization in scaffolds. In brief, the paraffin sections (3–5 µm) were dewaxed and immersed in water, and examined with a polarized light microscope (Olympus, Tokyo, Japan) after drying in air. The mineralization of the various nanofibrous scaffolds was evaluated by two experienced pathologists.

Confocal Raman Spectroscopy Analysis

Sample's preparation was similar to HE staining. In brief, the paraffin sections are carried by quartz slides to avoid interference by glass. Then the samples were dewaxed before being analyzed by confocal Raman spectroscopy (HOOKE Instruments Ltd, China). Samples were placed on the platform of a Raman spectrometer (HOOKE P300, HOOKE Instruments Ltd, China) for detection and spectral acquisition. The laser wavelength of Raman detection is 532 nm. The single spectrum acquisition condition is 5 mw for 3 s. 20 spectra were collected for each sample. The initial Raman spectra of all samples (7 * 4 = 28) were processed in batch using the software developed by Hooke (Hooke IntP), including: 1) developing the cosmic ray removal (CRR) algorithm to remove cosmic rays, and discriminating cosmic rays according to the formula: (test value-minimum) > (maximum credible value-Minimum) * Dynamic Factor; 2) Savitzky Golay convolution smoothing is used to smooth the Raman spectrum; 3) The background of Raman spectrum is removed by using airPLS algorithm; 4) Raman spectra were normalized according to the maximum peak. The Raman spectra were used to make the mean-variance diagram after pretreatment.

Histological Analysis of Inflammation Surrounding the Scaffolds

The preparation of histological samples was the same as described above. Tissue samples of various scaffolds were incised along the major axis and embedded in paraffin. Serial sections (3–5 μm) were used for hematoxylin and eosin (H&E) and immunohistochemistry staining. Olympus microscope BX51 and digital camera DP70 (Olympus, Tokyo, Japan) was used to photograph. Histological evaluation on all sections was performed by two independent examiners.

HE Staining and Inflammation Level Identifying

Images of the infiltrated cells surrounding mineralized and nonmineralized sites of P, PG, PH and PGH scaffold were captured using Olympus microscope BX51 and digital camera DP70. For analyzing HE stained sections, a refined inflammatory histological grading scale was used in this experiment (Table S1, Supporting Information).[39] Histological scoring for capsule quality: 4, fibrous, not dense, resembling connective or fat tissue; 3, fibrous, but immature, showing fibroblasts and little collagen; 2, granulous and dense, containing both fibroblasts and many inflammatory cells; 1, mass inflammatory cells with little or no signs of connective tissue organization; 0, cannot be evaluated because of infection or other factors. Histological scoring for capsule thickness: 4, 1−4 fibroblasts; 3, 5−9 fibroblasts; 2, 10−30 fibroblasts; 1, >30 fibroblasts; 0, not applicable. Histological scoring for cell infiltration: 4, only fibroblasts contact the surface; 3, scattered macrophages and leucocytes are present; 2, one layer of macrophages and leucocytes are present; 1, multiple layers of macrophages and leucocytes present; 0, cannot be evaluated. Infiltrated cells of four representative 20 × fields at the mineralized and non-mineralized sites of PH and PGH scaffold were evaluated per sample. Besides, four representative sites of P and PG group were also evaluated per sample as control.

Immunohistochemistry

Immunohistochemistry staining was performed as follows. Briefly, slides were dewaxed by incubation in a series of xylene, ethyl alcohol, and water. Then the slides were immersed in citric acid solution and heated to 95 °C for 15 min for antigen retrieval by microwave. After blocking endogenous peroxidase with 3% H_2O_2, the first antibody (IL-1α, TNFα, and CD68) were incubated over night at 4 °C. After rinsing with PBS for three times, the anti-rabbit/mouse HRP-labeled polymer was applied and incubated at 37 °C for 30 min. Staining was performed using diaminobenzidine tetrachloride (DAB) (Zymed Laboratories, San Francisco, CA, USA) by reacting with HRP of secondary antibody.

Statistical Analysis

All data were expressed as mean ± standard deviation (SD) and performed in at least 3 specimens. Statistical analysis was carried out using Student's t-test and one-way analysis of variance (ANOVA). A P value < 0.05 was considered statistically significant. The mean size of the fibers and the size distribution were calculated by analyzing 100 fibers from SEM images of the scaffolds by using ImageJ software (NIH, Bethesda, MD, USA). The initial Raman spectra were processed using the software developed by Hooke (Hooke IntP).

Acknowledgements

Conflict of Interest

The authors declare no conflict of interest.

Author Contributions

The manuscript was written through the contributions of all authors. All authors have given approval to the final version of the manuscript.

Open Research ⌄

Data Availability Statement

Research data are not shared.

Supporting Information

Filename	Description
[adhm202101586-sup-0001-SuppMat.pdf](#) 1.2 MB	Supporting Information

Please note: The publisher is not responsible for the content or functionality of any supporting information supplied by the authors. Any queries (other than missing content) should be directed to the corresponding author for the article.

References

1 G. H. Wilson 3rd, J. C. Gore, T. E. Yankeelov, S. Barnes, T. E. Peterson, J. M. True, S. Shokouhi, J. O. McIntyre, M. Sanders, V. Abramson, T. Q. Ngyuen, A. Mahadevan-Jansen, M. N. Tantawy, *J. Nucl. Med.* 2014, **55**, 1138.
Crossref | PubMed | Web of Science® | Google Scholar

2 D. K. Das, *Diagn. Cytopathol.* 2009, **37**, 534.
Wiley Online Library | PubMed | Web of Science® | Google Scholar

3 M. P. Reilly, M. L. Wolfe, A. R. Localio, D. J. Rader, *Atherosclerosis* 2004, **173**, 69.
Crossref | CAS | PubMed | Web of Science® | Google Scholar

4 H. J. Samvelyan, D. Hughes, C. Stevens, K. A. Staines, *Calcif. Tissue Int.* 2021, **109**, 243.
Crossref | CAS | PubMed | Web of Science® | Google Scholar

5 C. Rojulpote, A. J. Borja, V. Zhang, M. Aly, B. Koa, S. M. Seraj, W. Y. Raynor, E. Kothekar, F. Kaghazchi, T. J. Werner, O. Gerke, P. F. Hoilund-Carlsen, A. Alavi, *Am. J. Nucl. Med. Mol. Imaging* 2020, **10**, 47.
CAS | PubMed | Web of Science® | Google Scholar

6 S. J. Nyante, S. S. Lee, T. S. Benefield, T. N. Hoots, L. M. Henderson, *Cancer* 2017, **123**, 219.
Wiley Online Library | CAS | PubMed | Web of Science® | Google Scholar

7 M. H. M. Yunus, A. Nordin, H. Kamal, *Medicina* 2020, **56**, 614.
Crossref | Web of Science® | Google Scholar

8   M. A. Rogers, E. Aikawa, *Nat. Rev. Cardiol.* 2019, **16**, 261.

Crossref | CAS | PubMed | Web of Science® | Google Scholar

9   S. Rakoff-Nahoum, *Yale J. Biol. Med.* 2006, **79**, 123.

CAS | PubMed | Google Scholar

10   G. M. Tse, P. H. Tan, H. S. Cheung, W. C. Chu, W. W. Lam, *Breast Cancer Res. Treat.* 2008, **110**, 1.

Crossref | PubMed | Web of Science® | Google Scholar

11   E. Aikawa, M. Nahrendorf, J. L. Figueiredo, F. K. Swirski, T. Shtatland, R. H. Kohler, F. A. Jaffer, M. Aikawa, R. Weissleder, *Circulation* 2007, **116**, 2841.

Crossref | CAS | PubMed | Web of Science® | Google Scholar

12   A. Abdelbaky, E. Corsini, A. L. Figueroa, S. Fontanez, S. Subramanian, M. Ferencik, T. J. Brady, U. Hoffmann, A. Tawakol, *Circ.: Cardiovasc. Imaging* 2013, **6**, 747.

Crossref | PubMed | Web of Science® | Google Scholar

13   M. K. Haynes, E. L. Hume, J. B. Smith, *Clin. Immunol.* 2002, **105**, 315.

Crossref | CAS | PubMed | Web of Science® | Google Scholar

14   K. Gelse, S. Soder, W. Eger, T. Diemtar, T. Aigner, *Osteoarthritis Cartilage.* 2003, **11**, 141.

Crossref | CAS | PubMed | Web of Science® | Google Scholar

15   B. W. Hoyt, G. J. Pavey, B. K. Potter, J. A. Forsberg, *Bone* 2018, **109**, 3.

Crossref | PubMed | Web of Science® | Google Scholar

16   Z. Al-Aly, J. S. Shao, C. F. Lai, E. Huang, J. Cai, A. Behrmann, S. L. Cheng, D. A. Towler, *Arterioscler., Thromb., Vasc. Biol.* 2007, **27**, 2589.

Crossref | CAS | PubMed | Web of Science® | Google Scholar

17   S. E. New, C. Goettsch, M. Aikawa, J. F. Marchini, M. Shibasaki, K. Yabusaki, P. Libby, C. M. Shanahan, K. Croce, E. Aikawa, *Circ. Res.* 2013, **113**, 72.

Crossref | CAS | PubMed | Web of Science® | Google Scholar

18   J. F. Yan, W. P. Qin, B. C. Xiao, Q. Q. Wan, F. R. Tay, L. N. Niu, K. Jiao, *Biol. Rev.* 2020, **95**, 960.

Wiley Online Library | PubMed | Web of Science® | Google Scholar

19   T. Nakahara, M. R. Dweck, N. Narula, D. Pisapia, J. Narula, H. W. Strauss, *JACC: Cardiovasc. Imaging* 2017, **10**, 582.

Crossref | PubMed | Web of Science® | Google Scholar

20   B. Feng, H. C. Duan, W. Fu, Y. L. Cao, W. J. Zhang, Y. Z. Zhang, *J. Biomed. Mater. Res., Part A.* 2015, **103**, 431.

Wiley Online Library | CAS | PubMed | Web of Science® | Google Scholar

21   E. Ueda, P. A. Levkin, *Adv. Mater.* 2013, **25**, 1234.

Wiley Online Library | CAS | PubMed | Web of Science® | Google Scholar

22   N. Alexopoulos, P. Raggi, *Nat. Rev. Cardiol.* 2009, **6**, 681.

Crossref | CAS | PubMed | Web of Science® | Google Scholar

23   G. S. Abela, *J. Clin. Lipidol.* 2010, **4**, 156.

Crossref | PubMed | Web of Science® | Google Scholar

24   P. Maurovich-Horvat, U. Hoffmann, M. Vorpahl, M. Nakano, R. Virmani, H. Alkadhi, *JACC: Cardiovasc. Imaging* 2010, **3**, 440.

Crossref | PubMed | Web of Science® | Google Scholar

25   V. Gkretsi, T. Simopoulou, A. Tsezou, *Prog. Lipid Res.* 2011, **50**, 133.

Crossref | CAS | PubMed | Web of Science® | Google Scholar

26   F. Nudelman, K. Pieterse, A. George, P. H. Bomans, H. Friedrich, L. J. Brylka, P. A. Hilbers, G. de With, N. A. Sommerdijk, *Nat. Mater.* 2010, **9**, 1004.

Crossref | CAS | PubMed | Web of Science® | Google Scholar

27   C. P. Tarnowski, M. A. J. Ignelzi, M. D. Morris, *J. Bone Miner. Res.* 2002, **17**, 1118.

Wiley Online Library | PubMed | Web of Science® | Google Scholar

28   J. T. B. Ratnayake, M. Mucalo, G. J. Dias, *J. Biomed. Mater. Res., B* 2017, **105**, 1285.

Wiley Online Library | CAS | PubMed | Web of Science® | Google Scholar

29   R. Z. LeGeros, *Monogr. Oral Sci.* 1991, **15**, 109.

Google Scholar

30   D. J. Stechschulte Jr, D. C. Morris, S. F. Silverton, H. C. Anderson, H. K. Väänänen, *Bone Miner.* 1992, **17**, 187.

Crossref | CAS | PubMed | Web of Science® | Google Scholar

31   A. Trion, A. van der Laarse, *Am. Heart J.* 2004, **147**, 808.

Crossref | CAS | PubMed | Web of Science® | Google Scholar

32   E. Vey, C. Rodger, J. Booth, M. Claybourn, A. F. Miller, A. Saiani, *Polym. Degrad. Stab.* 2011, **96**, 1882.

Crossref | CAS | Web of Science® | Google Scholar

33 M. Therin, P. Christel, S. Li, H. Garreau, M. Vert, *Biomaterials* 1992, **13**, 594.

Crossref | CAS | PubMed | Web of Science® | Google Scholar

34 A. A. van Apeldoorn, H. J. van Manen, J. M. Bezemer, J. D. de Bruijn, C. A. van Blitterswijk, C. Otto, *J. Am. Chem. Soc.* 2004, **126**, 13226.

Crossref | CAS | PubMed | Web of Science® | Google Scholar

35 B. G. Frushour, J. L. Koenig, *Biopolymers* 1975, **14**, 379.

Wiley Online Library | CAS | PubMed | Web of Science® | Google Scholar

36 M. S. Shive, J. M. Anderson, *Adv. Drug Delivery Rev.* 1997, **28**, 5.

Crossref | CAS | PubMed | Web of Science® | Google Scholar

37 M. E. Bianchi, *J. Leukocyte Biol.* 2007, **81**, 1.

Wiley Online Library | CAS | PubMed | Web of Science® | Google Scholar

38 C. L. Holness, D. L. Simmons, *Blood* 1993, **81**, 1607.

Crossref | CAS | PubMed | Web of Science® | Google Scholar

39 J. A. Jansen, W. J. Dhert, J. P. van der Waerden, A. F. von Recum, *J. Invest. Surg.* 1994, **7**, 123.

Crossref | CAS | PubMed | Google Scholar

Download PDF

About Wiley Online Library

Privacy Policy
Terms of Use
About Cookies
Manage Cookies
Accessibility
Wiley Research DE&I Statement and Publishing Policies

Help & Support

Contact Us
Training and Support

DMCA & Reporting Piracy

Opportunities

Subscription Agents
Advertisers & Corporate Partners

Connect with Wiley

The Wiley Network
Wiley Press Room